Strong Sensitivity of Pine Island Ice-Shelf Melting to Climatic Variability

Pierre Dutrieux *et al.*

Science **343**, 174 (2014);
DOI: 10.1126/science.1244341

The model reasonably reproduces the Lyman-α plume morphology and brightness decrease with altitude (Fig. 3). At low altitudes (<100 km), the measured brightness decreases for both the Lyman-α and OI 130.4-nm emission. Because bright OI 135.6-nm emission is also detected up to altitudes of 200 km, the OI 130.4-nm profile might be best explained by a peak in O abundance at higher altitudes. Also, the derived plume height of 200 km is higher than expected from model results (*24*) and would require large supersonic eruption velocities of ~700 m/s. However, interpretation of the derived height and radial profile requires caution because of the systematic uncertainties of the disk location by one or two pixels or ~100 km. Moreover, a local density enhancement within a smooth global atmosphere would substantially alter the plasma environment, which in turn modifies the aurora morphology and brightness (*25*).

The high plume velocities and relatively low number densities we inferred are consistent with vapor emission from narrow fractures (*15*), as occurs at Enceladus (*23*, *26*). The surface area of Europa's fractures is too small to produce a thermal anomaly detectable by the Galileo Photopolarimeter-Radiometer instrument (*27*). Plume fallback could produce terrain softening in the near-polar regions, which might be detectable in suitable high-resolution images (*15*).

The modeled Lyman-α limb brightnesses for the 1999 and November 2012 geometries are not consistent with persistent plumes. Also, no striking surplus of OI 130.4-nm emission was detected. The model indicates that the plumes were less dense by at least a factor of 2 and 3 during the 1999 and November 2012 observations, respectively, if present (fig. S3). Thus, the plume activity appears to undergo considerable variability.

Recently, the plumes at Enceladus' south pole have been shown to be more active near the apocenter than at the pericenter (*28*). Similar tidal stress variability for Europa is expected to open and close its Linea features [fig. S4 (*15*)]. Europa was very close to its apocenter during the December 2012 observations and was shortly before and at the pericenter during the 1999 and November 2012 observations (Table 1). This causal relationship might explain the observed variability and the lack of detections in 1999 and November 2012. The plume variability, if real, verifies a key prediction of tidal-flexing models based on the existence of a subsurface ocean.

References and Notes

1. M. H. Carr *et al.*, *Nature* **391**, 363–365 (1998).
2. R. T. Pappalardo *et al.*, *J. Geophys. Res.* **104**, 24015–24055 (1999).
3. K. K. Khurana *et al.*, *Nature* **395**, 777–780 (1998).
4. B. E. Schmidt, D. D. Blankenship, G. W. Patterson, P. M. Schenk, *Nature* **479**, 502–505 (2011).
5. C. B. Phillips *et al.*, *J. Geophys. Res.* **105**, 22579–22597 (2000).
6. S. A. Fagents, *J. Geophys. Res.* **108**, 5139 (2003).
7. V. I. Shematovich, R. E. Johnson, J. F. Cooper, M. C. Wong, *Icarus* **173**, 480–498 (2005).
8. W. H. Smyth, M. L. Marconi, *Icarus* **181**, 510–526 (2006).
9. C. Plainaki *et al.*, *Icarus* **218**, 956–966 (2012).
10. D. T. Hall, D. F. Strobel, P. D. Feldman, M. A. McGrath, H. A. Weaver, *Nature* **373**, 677–679 (1995).
11. D. T. Hall, P. D. Feldman, M. A. McGrath, D. F. Strobel, *Astrophys. J.* **499**, 475–481 (1998).
12. M. A. McGrath, C. J. Hansen, A. R. Hendrix, in *Europa*, R. T. Pappalardo, W. B. McKinnon, K. K. Khurana, Eds. (Univ. of Arizona Press, Tucson, AZ, 2009), pp. 485–505
13. T. A. Cassidy, R. E. Johnson, M. A. McGrath, M. C. Wong, J. F. Cooper, *Icarus* **191**, 755–764 (2007).
14. J. Saur *et al.*, *Astrophys. J.* **738**, 153 (2011).
15. See the supplementary materials for more information.
16. Rayleigh (R) is the column emission rate of 10^{10} photons per square meter per column per second, 1 R = $10^{10}/4\pi$ photons m^{-2} sr^{-1} s^{-1}.
17. The 1999 Lyman-α image might hint at a plume feature in the south polar region (Fig. 1G), but is not statistically significant and is therefore not considered further.
18. C. A. Barth *et al.*, *Geophys. Res. Lett.* **24**, 2147–2150 (1997).
19. J. R. Spencer, L. K. Tamppari, T. Z. Martin, L. D. Travis, *Science* **284**, 1514–1516 (1999).
20. O. P. Makarov *et al.*, *J. Geophys. Res.* **109**, A09303 (2004).
21. J. Saur, D. F. Strobel, F. M. Neubauer, *J. Geophys. Res.* **103**, 19947–19962 (1998).
22. J. Zhang *et al.*, *Icarus* **163**, 182–197 (2003).
23. F. Tian, A. I. F. Stewart, O. B. Toon, K. W. Larsen, L. W. Esposito, *Icarus* **188**, 154–161 (2007).
24. S. A. Fagents *et al.*, *Icarus* **144**, 54–88 (2000).
25. L. Roth, J. Saur, K. D. Retherford, D. F. Strobel, J. R. Spencer, *Icarus* **214**, 495–509 (2011).
26. C. J. Hansen *et al.*, *Geophys. Res. Lett.* **38**, L11202 (2011).
27. J. A. Rathbun, N. J. Rodriguez, J. R. Spencer, *Icarus* **210**, 763–769 (2010).
28. M. M. Hedman *et al.*, *Nature* **500**, 182–184 (2013).

Acknowledgments: This work is based on HST observations available at the NASA Mikulski Archive for Space Telescopes. Support for program number GO-13040 was provided by NASA through a grant from the Space Telescope Science Institute, which is operated by the Association of Universities for Research in Astronomy, under contract NAS5-26555; and by Verbundforschung Astronomie und Astrophysik.

Supplementary Materials

www.sciencemag.org/content/343/6167/171/suppl/DC1
Materials and Methods
Supplementary Text
Figs. S1 to S10
Tables S1 to S2
References (*29*–*70*)

10 October 2013; accepted 2 December 2013
10.1126/science.1247051

Strong Sensitivity of Pine Island Ice-Shelf Melting to Climatic Variability

Pierre Dutrieux,[1]* Jan De Rydt,[1] Adrian Jenkins,[1] Paul R. Holland,[1] Ho Kyung Ha,[2] Sang Hoon Lee,[2] Eric J. Steig,[3] Qinghua Ding,[3] E. Povl Abrahamsen,[1] Michael Schröder[4]

Pine Island Glacier has thinned and accelerated over recent decades, significantly contributing to global sea-level rise. Increased oceanic melting of its ice shelf is thought to have triggered those changes. Observations and numerical modeling reveal large fluctuations in the ocean heat available in the adjacent bay and enhanced sensitivity of ice-shelf melting to water temperatures at intermediate depth, as a seabed ridge blocks the deepest and warmest waters from reaching the thickest ice. Oceanic melting decreased by 50% between January 2010 and 2012, with ocean conditions in 2012 partly attributable to atmospheric forcing associated with a strong La Niña event. Both atmospheric variability and local ice shelf and seabed geometry play fundamental roles in determining the response of the Antarctic Ice Sheet to climate.

Austral summer observations in the Amundsen Sea, West Antarctica, show that lightly modified, warm (0.5° to 1.2°C) and saline (>34.6) Circumpolar Deep Water (CDW), 2° to 4°C above the in situ freezing point, pervades a network of glacially scoured seabed troughs (*1*) (Fig. 1A). The CDW reaches nearby Antarctic glaciers and delivers heat to the base of their 200- to 1000-m-thick ice shelves (*2*–*4*). It is overlain by a 200- to 300-m-thick layer of cold (–1.5°C) and fresh (salinity <34.4) Winter Water (WW, Fig. 2A) that is seasonally replenished by interaction with the atmosphere and sea ice.

Pine Island Glacier (PIG), a major outlet glacier feeding one such ice shelf, has shown apparently continuous thinning (*5*, *6*) and intermittent acceleration (*7*–*9*) from 1973 to 2009. During this period, its ice shelf has also thinned (*6*, *10*–*12*), and the reduction in buttressing driven by oceanic melting is believed to be responsible for the changes inland. Earlier analysis indicated that a higher CDW volume and temperature in Pine Island Bay (PIB) in January 2009 caused an increase in ice-shelf melting and in the associated meltwater-driven circulation, relative to 1994 (*2*). The lack of subannual variability in CDW temperature during 1-year-long measurement in PIB (*1*) and the long-term correlation between the oceanic melting and the mass loss required to sustain thinning of the ice shelf gave the impression that the ice-ocean system had shown progressive change over the last two decades. This is consistent with a positive geometrical feedback, with oceanic melt enlarging the cavity under the ice shelf, allowing stronger circulation and further melting.

However, such ice-ocean systems are likely to be more complex. The glacier's rapid change

[1]British Antarctic Survey, Natural Environment Research Council (NERC), Cambridge, UK. [2]Korea Polar Research Institute, Korea Institute of Ocean Science and Technology (KIOST), Incheon, Korea. [3]Department of Earth and Space Sciences and Quaternary Research Center, University of Washington, Seattle, WA, USA. [4]Alfred-Wegener-Institute for Polar and Marine Research, Bremerhaven, Germany.

*Corresponding author. E-mail: pierre.dutrieux@bas.ac.uk

over the last few decades was probably triggered by its ungrounding from the top of a seabed ridge transverse to the ice flow at some time before the 1970s (*4*). Subsequent migration of the glacier's grounding line (*13*) down the seabed slope upstream from the ridge crest was probably an inevitable response (*14*), which had a major impact on cavity geometry, but projections of future evolution remain unclear (*15*–*17*). In this context, climate-driven variability of the delivery of heat to the ice-sheet margin may be important (*18*). To understand the relative roles of glacier dynamics and climate variability in driving past, present, and future glacier evolution requires knowledge of the spatial (*19*, *20*) (Fig. 1C) and temporal variability of ocean-driven melting.

Ocean simulations with a varying degree of horizontal resolution and using poorly constrained seabed and ice geometry produce a broad spectrum of variability in CDW volume in PIB (*21*) and oceanic melt of PIG (*22*). Some studies suggest that basal melt is sensitive to the strength of the circulation in the Amundsen Sea (*22*). Others associate its variability with changing wind-driven inflow of warm CDW at the continental shelf edge and temperature variability at the calving front of the glacier (*21*, *23*) influ-

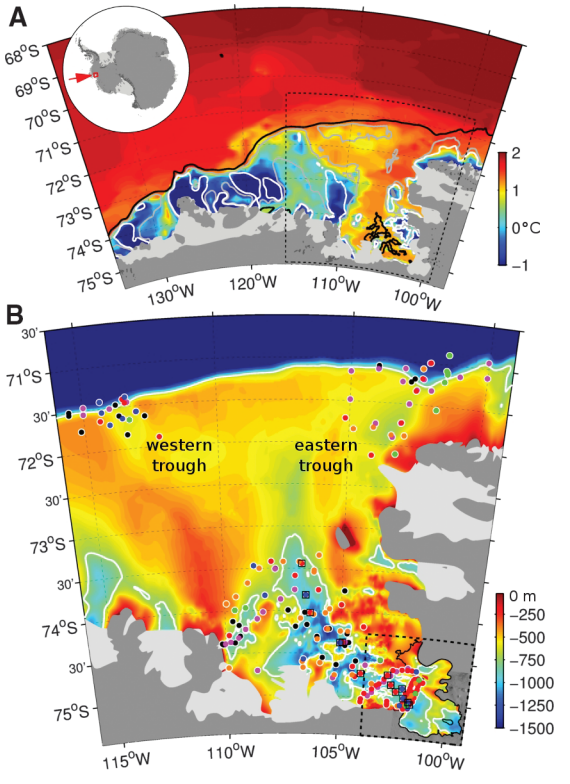

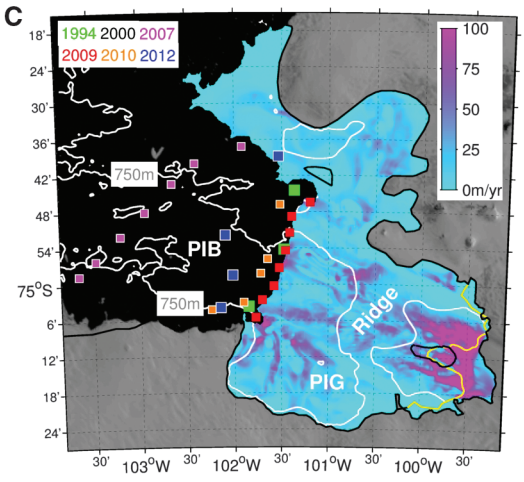

Fig. 1. Temperature maximum, seabed elevation, and selected observation locations in the Amundsen Sea. (**A**) Maximum subsurface temperature deduced from a climatology of observations taken between 1994 and 2012 (supplementary materials). Black, gray, and white contours indicate seabed elevations (*33*) of −1000, −500, and −400 m, respectively. The dashed black box shows the area in (B). (**B**) Detailed bathymetry on the eastern Amundsen Sea continental shelf. The white line shows −750-m seabed elevation. Color-coded dots (squares) show ocean station positions used in Fig. 2 (Fig. 3, A and B). The dashed black box shows the area in (C). The PIG ice shelf has been removed to show the seabed elevation beneath (supplementary materials). (**C**) The 2009 coastline and ice-shelf grounding line (*9*) are indicated by the black line. The yellow line shows the position of the grounding line in 1996 (*7*). Color-coded squares indicate ocean stations used to compute PIG ice shelf melt budgets. Simulated freshwater flux into the ocean (color) for 2009 boundary conditions.

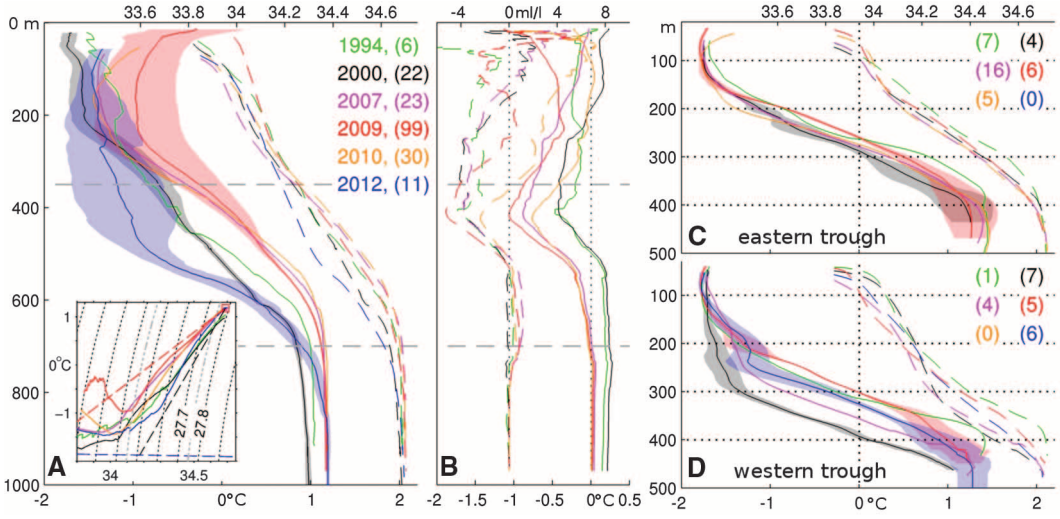

Fig. 2. Hydrographic properties in PIB. (**A**) Cruise-average, 25-dbar averaged temperature (continuous lines; shading indicates 1 SD for selected years) and salinity (dashed lines) profiles from January to March 1994, 2000, 2007, 2009, 2010, and 2012 in the wider Pine Island Bay (individual profile locations are shown in Fig. 1B; number of profiles per year is indicated in parentheses). Averages are performed in density-space and the resulting profiles re-gridded into pressure-space using the average stratification for each year. Dashed gray lines roughly indicate the 2009 ice-front draft and the seabed ridge crest, respectively. Inset: the same data in potential temperature-salinity space, with the surface freezing line indicated in dashed blue, the 2009 CDW-glacial-ice melt line in dashed red, and the 2009 CDW-WW mixing line in dashed black. Black-dotted contours of potential density anomaly are also shown, with the isopycnals corresponding to the 2009 ice-front draft and seabed ridge crest indicated in dotted gray. (**B**) Mean 2012 offset from other years in potential temperature (continuous) and meltwater concentration (dashed) for all other observed summers [color-coded as in (A)]. The difference is computed in density-space and then plotted in pressure-space using the mean 2009 stratification. (**C**) Same as (A), but for the near-shelf edge area to the east (see Fig. 1B). (**D**) Same as (A), but for the near-shelf edge area to the west (see Fig. 1B).

enced by far-field forcing of the atmospheric circulation (*18*). All these ocean-atmosphere sensitivities are linked dynamically, but a clear consensus on the most important driver of melt variability is lacking.

Hydrographic observations made in January 2012 in the eastern Amundsen Sea complement previous surveys from 1994, 2000, 2007, 2009 (*2*), and 2010 (*24*) (Fig. 1B) and offer a new perspective. Indeed, though near-bottom 2012 CDW temperatures of 1.2°C are very similar to the warmest records (2007, 2009, and 2010), the available heat reaching the PIG calving front is significantly reduced. The top of the thermocline (the depth at which temperature first increases sharply with increasing depth) is about 250 m deeper compared with that of any other year for which measurements exist (Figs. 2A and 3, A and B). Furthermore, the 2012 thermocline is sharpened such that the temperature increases from –0.8° to 0.8°C over only 180 m, compared with 250 to 350 m for other summers (Fig. 2A).

The temperature change occurring between 2010 and 2012 is largely associated with a salinity change, implying either that anomalies in the regional surface buoyancy or wind forcing cooled the upper thermocline through diapycnal exchanges (*25*) or that remote modifications in the atmosphere-ocean system led to decreased isopycnal advection of CDW from the continental shelf edge (*21*), or both. Thermocline depth changes in PIB are generally expected to occur at intraseasonal to interannual time scales (*21*, *22*), but the few synoptic summer observations available do not allow assessment of the origin, magnitude, frequency, or duration of such variability. Hydrographic profiles taken at the continental shelf edge in the troughs leading to PIB (Fig. 2, C and D) show that the western trough has a deeper and more variable thermocline than the eastern trough, consistent with the warmest inflows being found in the east (Fig. 1A), but heavy sea ice prevented sampling in the eastern trough in 2012.

Another observation is that a temperature decrease of 0.4° to 1°C occurred in 2012 at the location of previously identified meltwater outflows (*2*) (around 400-m depth, Fig. 2B), and this must be associated with changes in the ice shelf–ocean interaction. Derived ice-shelf meltwater concentrations (see supplementary materials) were 30 to 50% lower at these locations than during previous warm summers, and a weaker secondary meltwater maximum developed at around 600-m depth (Fig. 2B and fig. S3). The reduced meltwater concentration is identifiable in temperature-salinity space (Fig. 2A, inset), where previous warm summer observations depart far less from a two-component mixture of CDW and meltwater. Geostrophic budgets of dissolved oxygen, temperature, and salinity at the ice front (*26*) show that meltwater production dropped

Table 1. Balanced-transport estimates. For each set of observations, transports are estimated by balancing geostrophic fluxes of temperature, salinity, and dissolved oxygen budgets at the calving front of the ice shelf (see supplementary materials), allowing for a barotropic adjustment of the geostrophic velocity profiles (last column). Seawater transport into the cavity ("In") and net transport out of the cavity ("Diff", positive outward) are given in mSv (1 mSv = 10^3 m^3 s^{-1}) and in equivalent of ice (Iceq), using a water density of 1030 kg m^{-3} and an ice density of 920 kg m^{-3}. Meltwater transports are also shown, using the calculated meltwater fraction and balanced geostrophic velocity. Both transports do not depart significantly from each other, providing a consistency check. The 2007 observations were taken farther away from the ice front and thus are reflective of the entire ice shelf (*27*), whereas other years probably represent only the fast-flowing southern part of the ice shelf (see supplementary materials). Transport estimates are typically subject to a methodological uncertainty of about 10% (*2*).

Year	Seawater transport			Meltwater transport		Maximum (mean) correction
	mSv		km^3 $year^{-1}$ (Iceq)	km^3 $year^{-1}$ (Iceq)		cm s^{-1}
	In	Diff	Diff	In	Diff	
1994	–245	1.45	51.3	–36.4	49.1	2.8 (2.1)
2007	–355	3.13	110.6	–61.3	107.3	2.6 (0.8)
2009	–401	2.26	79.7	–36.8	79.4	2.4 (1.4)
2010	–401	2.13	75.2	–43.4	69.2	2.8 (2.1)
2012	–357	1.06	37.3	–71	34.7	1.6 (1.3)

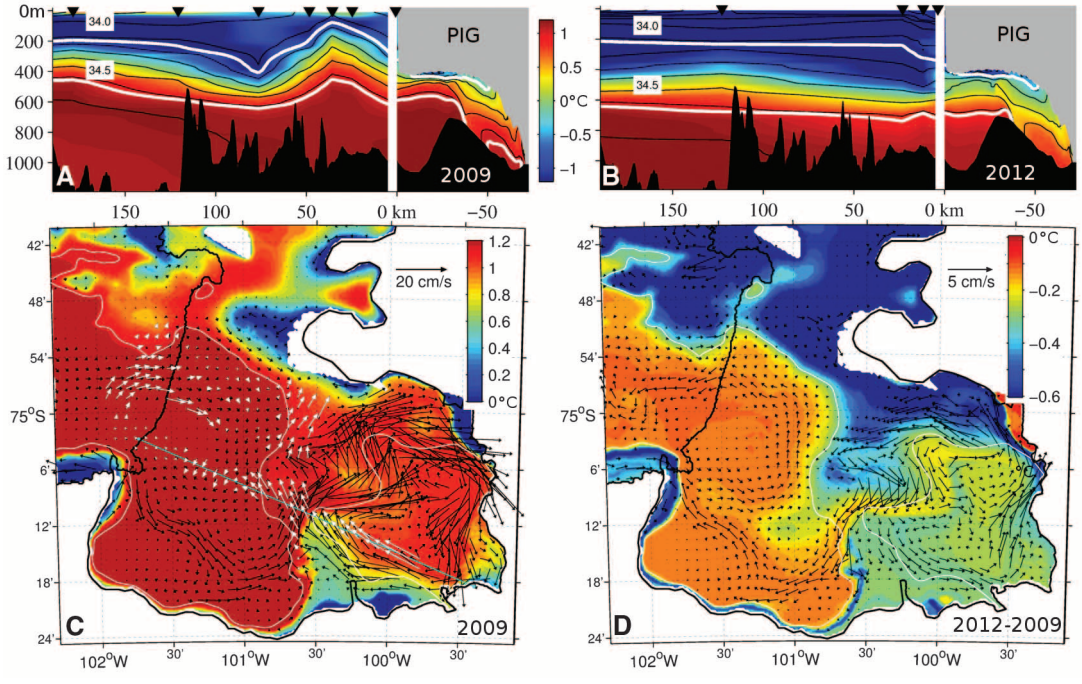

Fig. 3. Observed and simulated hydrography and circulation in 2009 and 2012. (**A**) Section of observed and simulated 2009 potential temperatures (color) and salinity (black contours) along the eastern Amundsen Sea trough and underneath the PIG ice shelf. White lines show the surface-referenced 27.47 and 27.75 isopycnals. The panel shows observations outside the PIG cavity, and simulation results within it. Observations are linearly interpolated from profiles (black triangles) indicated in Fig. 1B. (**B**) Same as (A) but for the 2012 observations and simulation. (**C**) Modeled potential temperature (color) and velocity (black vectors; every fifth vector is shown) averaged within 50 m of the seabed for the 2009 simulation. White vectors show the corresponding velocity observed by Autosub (binned on the model grid, see also fig. S2A). The cyan line indicates the position of the section used in (A) and (B). The white line indicates 750-m seabed depth. (**D**) Same as (C), but for the difference between the 2012 and the 2009 simulations.

from ~80 km^3 year^{-1} in 2009 (*2*) and 2010 (*24*) to 37 km^3 year^{-1} in 2012 (Table 1), assuming that synoptic sections are representative of a short-term balanced state. This amounts to a 53% decrease in meltwater production, making the basal melting of PIG in summer 2012 the lowest on record, even below that estimated in 1994, when the warmest, deepest waters were ~0.2°C cooler at the glacier front.

To clarify links between ocean and basal melt variability, we use a state-of-the-art regional ocean–ice shelf model at 400-m resolution with the latest ice and seabed geometry (see supplementary materials). When 2009 hydrographic conditions are imposed at its lateral boundaries (Fig. 3A), the model reproduces the main oceanographic features observed under the ice shelf by an autonomous submarine (*4*). The ocean circulation and water properties are divided in two by the ridge (Fig. 3, A and C). Offshore of the ridge, warm CDW circulates cyclonically after entering the cavity from the north, and then meanders back toward the ridge. Only the upper part of the CDW can flow over the ridge and reach the ice-shelf grounding line. This CDW melts the ice, creating a colder, fresher, buoyant meltwater plume that rises along the ice-shelf base (Fig. 3A). The vorticity created by this process and the cavity geometry impose a vigorous cyclonic circulation on the inshore side of the ridge, with near-seabed velocity reaching 0.2 m s^{-1} (Fig. 3C). The boundary between the inner and outer cavities is therefore marked by a dynamical front, further emphasizing (*2*, *4*) the crucial role played by the ridge in controlling the ocean circulation and its interaction with the ice shelf. For 2009, the model simulates reasonable basal melt patterns (Fig. 1C) compared with observations (*19*, *20*), producing 105 km^3 year^{-1} of meltwater over the entire ice shelf (*27*, *28*) and 86 km^3 year^{-1} over its more commonly quoted fast-flowing southern part (*2*, *19*, *24*) (see also supplementary materials).

In sensitivity experiments, 1994 and 2012 hydrographic conditions were imposed at the lateral boundaries while all other features (including ice geometry) were kept the same. For 2012, the simulated cooling of the sub-ice cavity and diminished basal melting are consistent with the observed decrease in meltwater production. The lowered thermocline in 2012 reduces the amount of heat flowing over the ridge and cools the water that reaches the grounding line by 0.3°C (Fig. 3B). In turn, melting is less pronounced and the buoyancy-driven circulation is concurrently decreased, particularly in the inner cavity (Fig. 3D). Overall, the model estimates a 31 to 38% decrease in meltwater flux from the ice shelf in response to the cooling at its boundaries (table S1). For 1994, when deepest waters are cooler than in 2012 but mid-depth waters are warmer, the model estimates only an 8 to 10% decrease in melting. These simulations neglect surface forcing and are limited by the imperfect seabed and constant ice geometry, which may explain the smaller reduction in melting than that observed. However, the model confirms the large sensitivity of the present ice-ocean system to the depth of the thermocline relative to the ridge that is implied by the observations. The inability of the simulation to proportionally reproduce the 1994 melting level also suggests the importance of unresolved changes in cavity geometry between 1994 and 2009 (*13*).

If prolonged, the ocean conditions observed in January 2012 would have profound implications for the PIG ice shelf. Continuation of a deep thermocline would reverse the current ice-shelf thinning (as ice advection overcompensates the weakened basal melt), potentially permitting a readvance of the grounding line. However, conditions in the months leading up to the 2012 observations were unusual (see also supplementary materials). Most of 2011 was marked by strong easterly wind anomalies over the Amundsen Sea (Fig. 4, A and B), weakening the typically cyclonic wind stress curl over the continental shelf (Fig. 4B) and curtailing the westerlies north of the shelf edge that are thought to enhance onshore CDW transport (*21*). Integrated over the preceding year, the zonal wind north of the continental shelf even reversed to easterly in 2011 (red line in Fig. 4B), an occurrence that is unique in the reanalysis wind record dating back to 1979. Such conditions potentially decreased the flux of CDW onto the continental shelf and enhanced coastal downwelling, creating the 2012 thermohaline configuration with a relatively thin CDW layer in PIB.

The wind variability over the Amundsen Sea has both local and remote origins. In particular, convective anomalies in the equatorial Pacific troposphere are known to radiate an atmospheric wave train toward the area (*29*), affecting winds at the continental shelf edge. The strong easterly anomaly in January 2012 can be attributed to exceptionally weak convection in the western tropical Pacific associated with a major La Niña event developing in late 2011 (Fig. 4C). The relevance of remote forcing from the tropical Pacific is illustrated by the statistically significant correlation (0.48) between the Niño 3.4 sea-surface temperature (SST) anomaly and the zonal wind over the continental shelf edge (Fig. 4A, see also supplementary materials). Although other factors affect the thermohaline structure in PIB, such as eddy variability at the shelf edge (*30*), coastal downwelling (*1*), and buoyancy forcing (*25*, *26*, *31*), the conjunction of the January 2012 ocean conditions and the atmospheric anomalies in the preceding months confirms the important

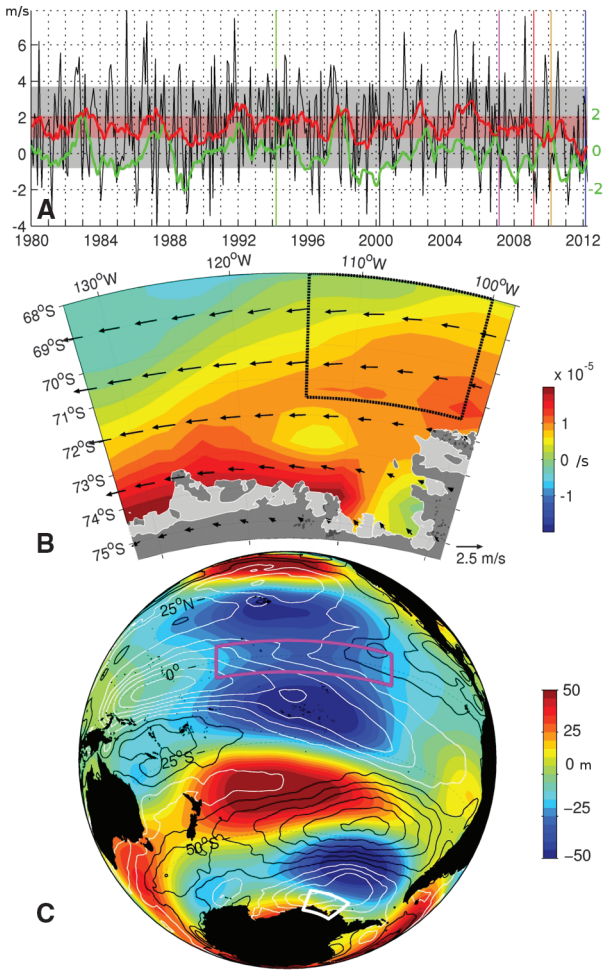

Fig. 4. Exceptional forcing before the 2012 anomaly. (**A**) Monthly-mean 10-m-height zonal wind velocity (*34*) (black) and its running integral over the preceding 12 months (red), averaging over the area indicated by the black-dotted box in (B). Shaded areas indicate 1 SD around the mean for each. The green line shows the sea-surface temperature monthly anomaly in the Niño 3.4 area. Dates of ocean observations are indicated by colored vertical lines. (**B**) 2011 annual mean of anomalies in surface wind (vector) and wind-stress curl (color) with respect to the 1979–2011 monthly climatology of each. (**C**) 2011 annual mean of anomalies in atmospheric geopotential height at 200 hPa (color) and sea surface zonal wind (contour) with respect to the 1979–2011 monthly climatology. White (black) contour are negative (positive), with 1 m s^{-1} interval. The white and magenta boxes indicate the area depicted in (B) and the Niño 3.4 area, respectively.

role of tropical forcing in determining the variability of melt rates under the PIG ice shelf (*18*).

Neighboring ice shelves closer to the continental shelf edge and exposed to greater ocean variability are naturally prone to a larger variability in melting (*32*). However, the presence of the ridge in front of the grounding line of PIG enhances its sensitivity to changes in oceanic and climatic forcing. Specifically, the blocking effect of the ridge makes the vertical distribution of heat a key element of the melting response. This study therefore stresses the importance of both local geometry and climate variability in determining ice-shelf melting. With the added realization that this melting varies appreciably over kilometer scales (*19*, *20*) and that oceanic variability is expected on intraseasonal to interannual time scales, it is clear that progress in the understanding and prediction of ice-sheet contributions to sea-level rise requires observations and models that capture a wide range of spatial and temporal scales.

References and Notes

1. S. S. Jacobs *et al.*, *Oceanography* **25**, 154–163 (2012).
2. S. S. Jacobs, A. Jenkins, C. F. Giulivi, P. Dutrieux, *Nat. Geosci.* **4**, 519–523 (2011).
3. S. S. Jacobs, H. H. Hellmer, A. Jenkins, *Geophys. Res. Lett.* **23**, 957–960 (1996).
4. A. Jenkins *et al.*, *Nat. Geosci.* **3**, 468–472 (2010).
5. D. J. Wingham, D. W. Wallis, A. Shepherd, *Geophys. Res. Lett.* **36**, L17501 (2009).
6. A. Shepherd *et al.*, *Science* **338**, 1183–1189 (2012).
7. E. Rignot, *Geophys. Res. Lett.* **35**, L12505 (2008).
8. I. Joughin, E. Rignot, C. E. Rosanova, B. K. Lucchitta, J. Bolhander, *Geophys. Res. Lett.* **30**, 1706 (2003).
9. I. Joughin, B. E. Smith, D. M. Holland, *Geophys. Res. Lett.* **37**, L20502 (2010).
10. H. D. Pritchard *et al.*, *Nature* **484**, 502–505 (2012).
11. A. Shepherd *et al.*, *Geophys. Res. Lett.* **37**, L13503 (2010).
12. A. Shepherd, D. Wingham, E. Rignot, *Geophys. Res. Lett.* **31**, L23402 (2004).
13. J. W. Park *et al.*, *Geophys. Res. Lett.* **40**, 2137–2142 (2013).
14. C. Schoof, *J. Geophys. Res.* **112**, F03S28 (2007).
15. S. S. R. Jamieson *et al.*, *Nat. Geosci.* **5**, 799–802 (2012).
16. G. H. Gudmundsson, J. Krug, G. Durand, L. Favier, O. Gagliardini, *Cryosphere* **6**, 1497–1505 (2012).
17. R. M. Gladstone *et al.*, *Earth Planet. Sci. Lett.* **333-334**, 191–199 (2012).
18. E. J. Steig, Q. Ding, D. S. Battisti, A. Jenkins, *Ann. Glaciol.* **53**, 19–28 (2012).
19. P. Dutrieux *et al.*, *Cryosphere* **7**, 1543–1555 (2013).
20. T. P. Stanton *et al.*, *Science* **341**, 1236–1239 (2013).
21. M. Thoma, A. Jenkins, D. Holland, S. Jacobs, *Geophys. Res. Lett.* **35**, L18602 (2008).
22. M. P. Schodlok, D. Menemenlis, E. Rignot, M. Studinger, *Ann. Glaciol.* **53**, 156–162 (2012).
23. P. Heimbach, M. Losch, *Ann. Glaciol.* **53**, 59–69 (2012).
24. Y. Nakayama, M. Schröder, H. H. Hellmer, *Deep Sea Res. Part I Oceanogr. Res. Pap.* **77**, 50–62 (2013).
25. A. A. Petty, D. L. Feltham, P. R. Holland, *J. Phys. Oceanogr.* **43**, 920–940 (2013).
26. P. R. Holland, A. Jenkins, D. M. Holland, *J. Geophys. Res.* **115**, C05020 (2010).
27. E. Rignot, S. Jacobs, J. Mouginot, B. Scheuchl, *Science* **341**, 266–270 (2013).
28. M. A. Depoorter *et al.*, *Nature* **502**, 89–92 (2013).
29. Q. Ding, E. J. Steig, D. S. Battisti, M. Küttel, *Nat. Geosci.* **4**, 398–403 (2011).
30. P. St-Laurent, J. M. Klinck, M. S. Dinniman, *J. Phys. Oceanogr.* **43**, 51–64 (2013).
31. L. Padman *et al.*, *J. Geophys. Res.* **117**, C01010 (2012).
32. S. S. Jacobs *et al.*, *J. Geophys. Res. Ocean.* **118**, 4152–4168 (2013).
33. R. Timmermann *et al.*, *Earth Syst. Sci. Data* **2**, 261–273 (2010).
34. D. P. Dee *et al.*, *Q. J. R. Meteorol. Soc.* **137**, 553–597 (2011).

Acknowledgments: P.D. and J.D.R. were supported by Natural Environment Research Council grants NE/G001367/1, NE/H02333X/1, and NE/J005770/1. H.K.H. and S.H.L. were supported by Korea Polar Research Institute grants PP12010 and PP13020. The European Centre for Medium-Range Weather Forecasts is acknowledged for serving the ERA-Interim reanalysis data set, and Center for Remote Sensing of Ice Sheets (with support from NSF grant ANT-0424589 and NASA grant NNX10AT68G) is acknowledged for generating and serving radar observations.

Supplementary Materials

www.sciencemag.org/content/343/6167/174/suppl/DC1
Materials and Methods
Figs. S1 to S10
Tables S1
References (*35*–*60*)

6 August 2013; accepted 6 December 2013
Published online 2 January 2014;
10.1126/science.1244341

A Spatial Accommodation by Neighboring Cells Is Required for Organ Initiation in *Arabidopsis*

Joop E. M. Vermeer,[1*] Daniel von Wangenheim,[2,3] Marie Barberon,[1] Yuree Lee,[1] Ernst H. K. Stelzer,[2] Alexis Maizel,[3] Niko Geldner[1*]

Lateral root formation in plants can be studied as the process of interaction between chemical signals and physical forces during development. Lateral root primordia grow through overlying cell layers that must accommodate this incursion. Here, we analyze responses of the endodermis, the immediate neighbor to an initiating lateral root. Endodermal cells overlying lateral root primordia lose volume, change shape, and relinquish their tight junction–like diffusion barrier to make way for the emerging lateral root primordium. Endodermal feedback is absolutely required for initiation and growth of lateral roots, and we provide evidence that this is mediated by controlled volume loss in the endodermis. We propose that turgidity and rigid cell walls, typical of plants, impose constraints that are specifically modified for a given developmental process.

Epithelia are central to multicellular life. Their ringlike paracellular barriers separate different environments, and their polar surfaces mediate selective and vectorial uptake of substances (*1*). The crucial barrier function of epithelia must be maintained during growth and development. In animals, epithelial remodeling involves a complex, supracellular interplay of force generating cytoskeleton and dynamically remodeled adherens junctions (*2*). In plants, the root endodermis has a function very similar to that of animal epithelia, yet its independent evolution in the context of a multicellular organism with turgid, wall-bearing, nonmotile cells has led to profoundly different cellular structures (*3*). Instead of being mediated by direct protein-protein interactions, the paracellular diffusion barrier of the endodermis is set up by the Casparian strips, ringlike, hydrophobic impregnations of the primary cell wall that fuse into a supracellular network between endodermal cells. These impregnations consist of lignin, an inelastic phenolic polymer that is resistant to chemical degradation (*4*). The Casparian strip establishment is locally guided by the Casparian strip domain proteins (CASPs). These transmembrane proteins, which form a ring-like plasma membrane subdomain, establish a lateral diffusion barrier and recruit biosynthetic enzymes for Casparian strip formation (*5*, *6*). Yet, despite the presence of a Casparian strip, the endodermis has to be remodeled during lateral root formation.

Lateral roots are formed from the pericycle, a cell layer located deep within the primary root, confined between the vascular bundle and the endodermis. As the lateral root primordium grows, it has to traverse the endodermis, cortex, and epidermis in order to emerge from the primary root. The hormone auxin triggers lateral root development and also signals to the overlying cell layers (*7*). Outer cortex and epidermal cell layers assist lateral root emergence after auxin from the lateral root primoridum triggers degradation of the SOLITARY-ROOT repressor protein, which permits expression of pectinases that disrupt intercellular adhesions (*8*, *9*). The endodermis, however, must be breached first, and its Casparian strip network cannot be degraded by pectinases. An-

[1]Department of Plant Molecular Biology, Biophore, UNIL-Sorge, University of Lausanne, 1015 Lausanne, Switzerland. [2]Buchmann Institute for Molecular Life Sciences, Goethe University Frankfurt, D-60438 Frankfurt Am Main, Germany. [3]Center for Organismal Studies, University of Heidelberg, D-69120 Heidelberg, Germany.

*Corresponding author. E-mail: joop.vermeer@unil.ch (J.E.M.V.); niko.geldner@unil.ch (N.G.)